CELL BIOLOGY

Molecular insights into the human CLC-7/Ostm1 transporter

Sensen Zhang[1]*, Yang Liu[1]*, Bing Zhang[2]*, Jun Zhou[1]*, Tianyu Li[3], Zhiqiang Liu[2†], Yang Li[3†], Maojun Yang[1,4†]

CLC family proteins translocate chloride ions across cell membranes to maintain the membrane potential, regulate the transepithelial Cl^- transport, and control the intravesicular pH among different organelles. CLC-7/Ostm1 is an electrogenic Cl^-/H^+ antiporter that mainly resides in lysosomes and osteoclast ruffled membranes. Mutations in human CLC-7/Ostm1 lead to lysosomal storage disorders and severe osteopetrosis. Here, we present the cryo–electron microscopy (cryo-EM) structure of the human CLC-7/Ostm1 complex and reveal that the highly glycosylated Ostm1 functions like a lid positioned above CLC-7 and interacts extensively with CLC-7 within the membrane. Our complex structure reveals a functionally crucial domain interface between the amino terminus, TMD, and CBS domains of CLC-7. Structural analyses and electrophysiology studies suggest that the domain interaction interfaces affect the slow gating kinetics of CLC-7/Ostm1. Thus, our study deepens understanding of CLC-7/Ostm1 transporter and provides insights into the molecular basis of the disease-related mutations.

INTRODUCTION

The CLC family comprises a group of integral membrane proteins that translocate Cl^- across the cell membranes; members of this family are essential for the maintenance of membrane potential, regulation of transepithelial Cl^- transport, and control of intravesicular pH (*1*–*3*). Human CLC proteins can be divided into two subtypes. The first subtype consists of Cl^- channels: CLC-1, CLC-2, CLC-Ka, and CLC-Kb, which are mainly found at the cell membrane, where they function to control the Cl^- flow and to stabilize the membrane potential (*4*). The remaining CLC proteins (CLC-3 to CLC-7) are electrogenic Cl^-/H^+ antiporters (*5*–*8*) that exchange Cl^- and H^+ with a stoichiometry of 2:1. CLC proteins function as dimers, with each subunit having its own passageway for ion transport (*9*–*15*). Previous macroscopic current and single-channel studies have indicated that CLC proteins apparently display two distinct types of gating process (*9*, *16*, *17*): fast gating ("protopore gate"), wherein the ion-conducting pore of one subunit opens and closes independently of the other subunit and which is thought to result largely from a small movement of the gate glutamate residue positioned within the ion-conducting pore, and slow gating ("common gate"), which operates both pores simultaneously. The detailed mechanism underlying the slow gating process remains mysterious.

CLC-7 functions as an electrogenic antiporter that mainly resides in lysosomes and osteoclast ruffled membranes (*18*–*20*). Accumulating evidence suggests that Ostm1 serves as an ancillary β subunit of CLC-7 to support bone resorption and lysosomal function (*7*, *19*). The specific H^+ concentration in the lysosome is mainly achieved through proton pump V-type H^+-dependent adenosine triphosphatases (H^+-ATPases) (*21*), and the physiological role of CLC-7 in lysosomal acidification remains controversial (*1*). Initially, CLC-7 was suggested to provide a means for charge-compensating conductance for proton pumping, thereby facilitating lysosomal acidification (*22*). However, later studies established that lysosomal pH is normal in *Clcn7*$^{-/-}$ and *Ostm1*$^{-/-}$ mice (*18*, *19*, *23*), suggesting that the major role of CLC-7 is to increase the luminal Cl^- concentration by exploiting the proton gradient created by H^+-ATPase, rather than providing a shunting conductance. In addition, a study reporting the identification of a gain-of-function mutation (Y715C) in CLC-7 that alters lysosomal pH (*24*) provides additional evidence to support a functional role for CLC-7 in regulating lysosomal pH. It is thus clear that further studies are required to elucidate the physiological role of CLC-7 transporter.

In the clinic, mutations in human CLC-7 and Ostm1 are known to cause severe osteopetrosis and lysosomal storage disorder (*18*–*20*, *25*). Osteopetrosis is a severe hereditary disorder characterized by increased bone density and abnormal bone growth due to resorption defects (*26*, *27*). To date, clinical investigations of patients with osteopetrosis have identified pathogenesis-related mutations in at least eight genes, including *TCIRG1*, *CLCN7*, *OSTM1*, *PLEKHM1*, *SNX10*, *TNFSF11*, *TNFRSF11A*, and *CAII* (*28*). Apart from increased bone density phenotypes, patients with malignant osteopetrosis always develop micrognathia, hydrocephalus, cranial nerve compression, frontal bossing, eye protrusion, and choanal stenosis (*26*, *27*).

Although some CLC transporters (EcCLC and CmCLC) have been extensively studied (*11*, *12*), the molecular details of human Cl^-/H^+ transporter have not been characterized yet. Here, we present the structure of the human CLC-7/Ostm1 complex and reveal that the highly glycosylated Ostm1 subunit surrounds the intravesicular domain and transmembrane domain (TMD) of CLC-7. Further, we couple our structural insights with electrophysiology studies to confirm that domain interface residues of CLC-7 function to regulate slow gating kinetics. The complex structure, together with our electrophysiology studies of CLC-7/Ostm1, deepens understanding of the slow gating mechanism of CLC family and lays a foundation for interpreting the etiopathology of known disease-related mutations.

[1]Ministry of Education Key Laboratory of Protein Science, Tsinghua-Peking Joint Center for Life Sciences, Beijing Advanced Innovation Center for Structural Biology, School of Life Sciences, Tsinghua University, Beijing 100084, China. [2]Department of Anesthesiology, Shanghai First Maternity and Infant Hospital, Tongji University School of Medicine, Shanghai 201204, China. [3]CAS Key Laboratory of Receptor Research, Shanghai Institute of Materia Medica, Chinese Academy of Sciences, Shanghai 201203, China. [4]School of Pharmacy, Tongji Medical College, Huazhong University of Science and Technology, Wuhan 430030, China.
*These authors contributed equally to this work.
†Corresponding author. Email: drliuzhiqiang@163.com (Z.L.); liyang@simm.ac.cn (Y.L.); maojunyang@tsinghua.edu.cn (M.Y.)

RESULTS

Overall structure of the human CLC-7/Ostm1 complex

To obtain abundant and homogeneous proteins suitable for our cryo–electron microscopy (cryo-EM) study, human CLC-7 and Ostm1 were coexpressed using the BacMam virus expression system (fig. S1) and subsequently reconstituted in digitonin micelle buffer. Ultimately, we determined the structure of the CLC-7/Ostm1 complex to a resolution of 3.7 Å, allowing confident model building for most of the protein regions (figs. S1 and S2 and table S1). The C2 symmetrical architecture of CLC-7/Ostm1 complex contains two CLC-7 and two Ostm1 monomers, with overall dimensions of 110 Å × 120 Å × 70 Å (Fig. 1, A and B).

In agreement with previously resolved CLC proteins (*11*–*15*), CLC-7 adopts a dimeric architecture with each monomer consisting of 24 α helices and 5 β strands (Fig. 1C). The transmembrane region of the complex consists of two independent hourglass-shaped transport pathways constricted by selectivity filters (Fig. 1B). Each monomer contains two cystathionine-β-synthase subdomains (CBS1 and CBS2), which are tightly packed against each other through a pseudo-twofold symmetry axis (Fig. 1B). The dimeric ancillary β subunits Ostm1 surround the CLC-7 dimer at the TMD and the intravesicular regions (Fig. 1, A and B). The single transmembrane helix of Ostm1 is located adjacent to helices C, J, and K of each CLC-7 monomer, while the Ostm1 intravesicular domain lays above the CLC-7 TMDs (Fig. 1B). The intravesicular domain of Ostm1 comprises six helices (EH1 to EH6), with EH1 to EH3 positioned in the center of the intravesicular domain and EH4 to EH6 positioned close to Ostm1's own TMD (Fig. 1D). Neither the N terminus (32–72) nor the C terminus (309–334) of Ostm1 exhibited discernible density, indicating a possibly disordered structure and/or conformational flexibility.

Ostm1 as a lid above CLC-7

The rhombus-shaped intravesicular domain of Ostm1 is positioned directly above CLC-7, appearing like a lid (Fig. 1, A and B). A previous study has indicated that the intravesicular domain of Ostm1 was linked via disulfide bonds (*19*). Our complex structure enabled identification of three pairs of disulfide bonds within the intravesicular domain that help to stabilize its structure. Cys^{84} of EH1 interacts with Cys^{142} on the loop between EH2 and EH3; Cys^{101} of EH1 interacts with Cys^{115} on EH2; Cys^{112} on the loop between EH1 and EH2 interacts with Cys^{171} on the loop between EH3 and EH4 (Fig. 2A). These observable disulfide bonds in the solved structure are within a single Ostm1 monomer, but not between different Ostm1 monomers, findings consistent with a previous study (*19*). These cysteines are well conserved among different species (fig. S3), supporting their potential roles in stabilizing the Ostm1 intravesicular domain.

In addition to the conserved disulfide bonds in the intravesicular domain, we also observed seven glycosylation modifications on Ostm1 asparagine residues (Asn^{93}, Asn^{128}, Asn^{163}, Asn^{184}, Asn^{194}, Asn^{216}, and Asn^{263}) (Fig. 2B). It has long been recognized that the extensive glycosylation modifications help to protect lysosomal membrane proteins from degradation by hydrolases (*19*, *29*). While most of the glycosylation modifications (Asn^{93}, Asn^{128}, Asn^{184}, Asn^{194}, and Asn^{216}) identified in our structure protrude toward the intravesicular side, it is noteworthy that two of the dendritic glycan moieties [Asn^{163}-N-acetylglucosamine (NAG) and Asn^{263}-N-acetylglucosamine (NAG)] stretch into the cleft between Ostm1 and CLC-7, thereby filling

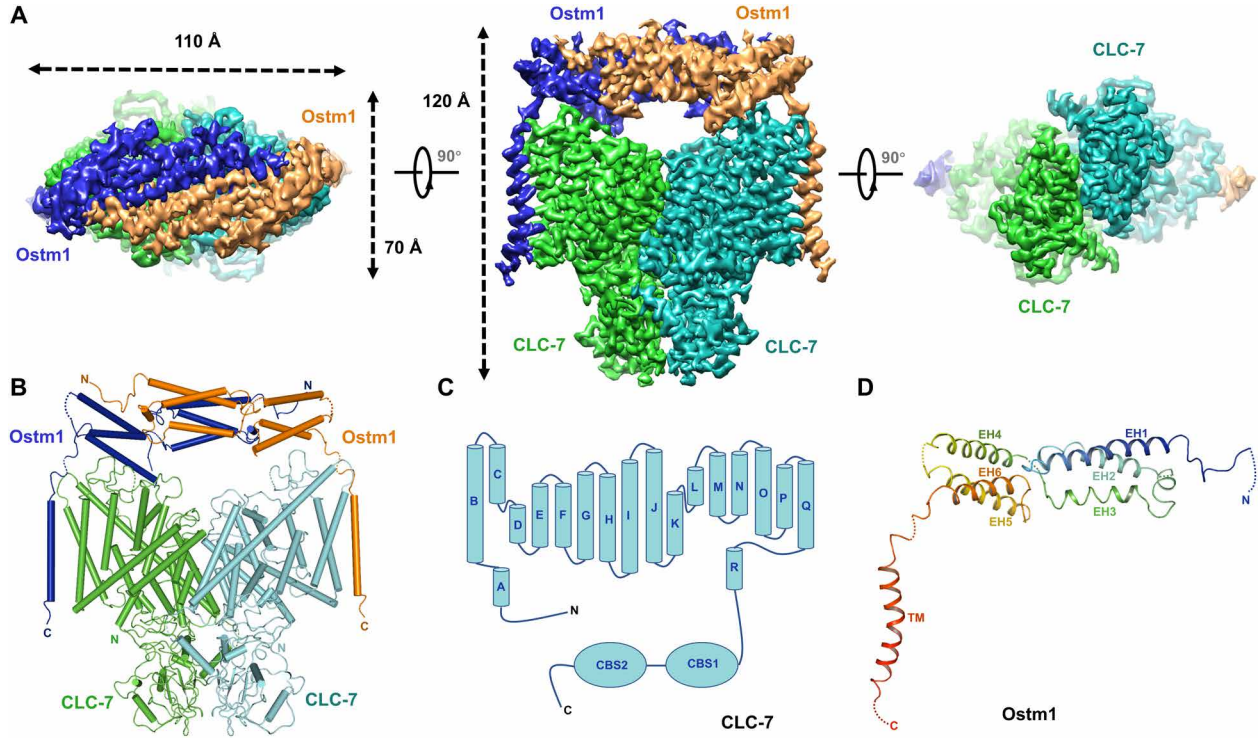

Fig. 1. Structure of the CLC-7/Ostm1 complex. (**A**) Cryo-EM map of the CLC-7/Ostm1 complex from three views (from left to right: top view, side view, and bottom view), with each subunit color-coded (green and cyan for CLC-7, blue and brown for Ostm1). (**B**) Cartoon representation of the CLC-7/Ostm1 complex from the side view, with each subunit color-coded as in (A). (**C**) Topology diagram of CLC-7. (**D**) Ribbon representation of the Ostm1 monomer, colored by structural element.

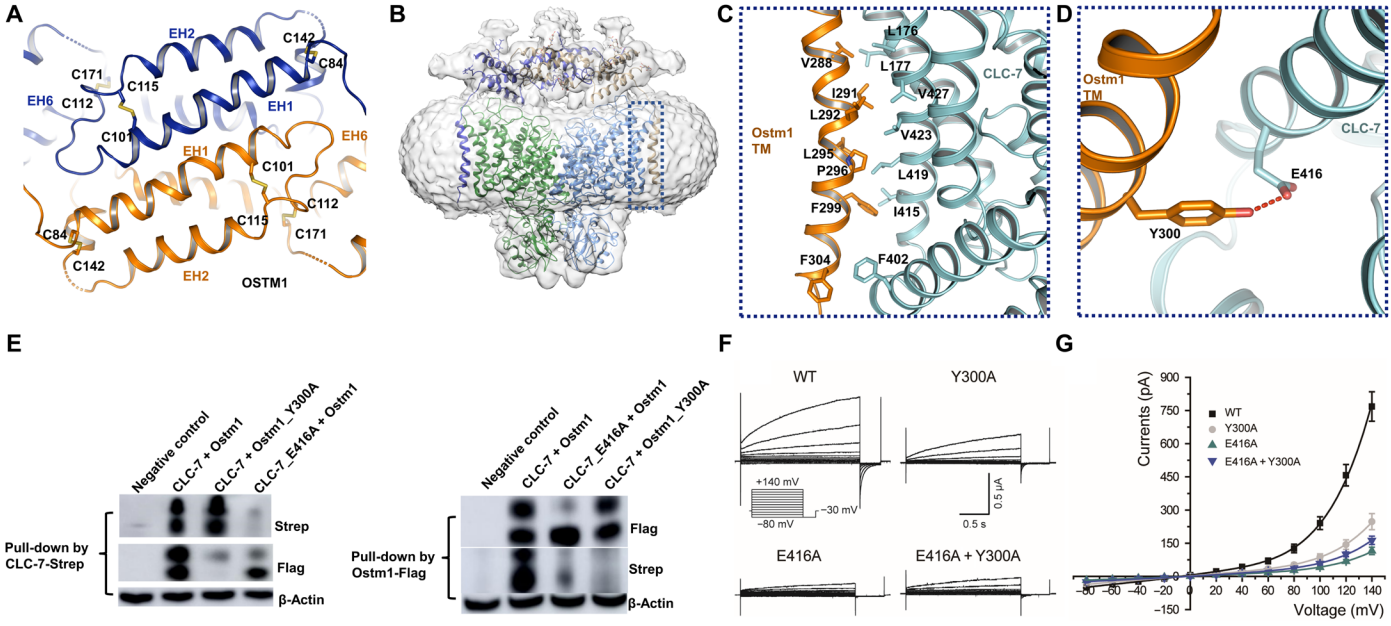

Fig. 2. The intravesicular domain of Ostm1. (**A**) Three pairs of disulfide bonds (Cys^{84}-Cys^{142}, Cys^{101}-Cys^{115}, and Cys^{112}-Cys^{171}) were observed in the intravesicular domain of Ostm1. (**B**) Schematic representation of the CLC-7/Ostm1 complex docked into the cryo-EM density map from a side view. Glycosylation modification sites were indicated in the intravesicular domain of Ostm1. (**C**) Hydrophobic interactions between the transmembrane regions of CLC-7 and Ostm1. (**D**) Magnified view of the polar interaction between the TMD of CLC-7 and Ostm1. Glu^{416} in the helix K of CLC-7 interacts with Tyr^{300} of Ostm1. (**E**) In vitro pull-down assays using Strep-tagged CLC-7 as a bait protein (left) or using Flag-tagged Ostm1 as a bait protein (right). Substituting $Ostm1^{Y300}$ and $CLC\text{-}7^{E416}$ to alanine decreased complex stability. (**F**) Representative current traces of the WT and mutant CLC-7/Ostm1 in Chinese hamster ovary cells. WT and mutant CLC-7 additionally carry the leucine mutation that could partially target CLC-7 to plasma membrane (*7*). Voltage was clamped from −80 to +140 mV in 2-s steps of 20 mV (inset). (**G**) *I-V* curves of the mutants that were shown in (F). $n = 16$, 13, 11, and 10 for WT, $Ostm1^{Y300A}$, $CLC\text{-}7^{E416A}$, and $CLC\text{-}7^{E416A}$/$Ostm1^{Y300A}$, respectively.

in the contact surface (fig. S4, A and B). For the large intravesicular domain, the Ostm1 dimeric interface is formed from EH1 and EH3 of one Ostm1 monomer situated close to the neighboring EH1 and EH3 of the second Ostm1 monomer (fig. S4C). We also noted that the intravesicular domain of Ostm1 is also stabilized by a hydrogen bond between Glu^{168} of one Ostm1 monomer with Arg^{151} of the second Ostm1 monomer (fig. S4D).

Interactions between CLC-7 and Ostm1

Examination of the complex structure emphasized that the interaction between CLC-7 and Ostm1 was mainly contributed by these proteins' TMDs. Specifically, the transmembrane segments of Ostm1 interact with transmembrane helices C, J, and K of CLC-7 via extensive hydrophobic interactions (Fig. 2C) that are mediated by conserved residues (fig. S3). In addition to the hydrophobic interaction, the hydroxyl group of Tyr^{300} on the single transmembrane helix of Ostm1 forms a hydrogen bond with the carboxylic group of Glu^{416} on helix K of CLC-7 (Fig. 2D). Moreover, within the cleft between the Ostm1 intravesicular domain and the CLC-7 intravesicular domain, EH5 of Ostm1 interacts with the loop intervening helices K and L of CLC-7 via a hydrogen bond mediated by Tyr^{228} from Ostm1 and Asp^{456} from CLC-7 (fig. S4D).

The essential role of the interactions between CLC-7 and Ostm1 TMDs was demonstrated in a previous study (*7*) that the TMD of Ostm1 bound with CLC-7 and was required for transport activity. Seeking experimental validation for some of the interacting residues identified in our structure that enable this essential binding between the TMDs, we performed in vitro pull-down assays with extracts from cells coexpressing strep-tagged CLC-7 and Flag-tagged Ostm1. As illustrated in fig. S5A, the $CLC\text{-}7^{E416A}$ mutation resulted in a remarkably reduced protein level compared with wild-type (WT) CLC-7, while the $Ostm1^{Y300A}$ mutation retained almost the same protein level to that of WT Ostm1. Substituting $Ostm1^{Y300}$ and $CLC\text{-}7^{E416}$ to alanine decreased complex stability in both the strep-mediated and Flag-mediated in vitro pull-down assays (Fig. 2E).

Having confirmed that the $Ostm1^{Y300A}$ and $CLC\text{-}7^{E416A}$ mutants reduce the stability of the complex at the membrane, we next expressed these mutants in Chinese hamster ovary (CHO) cells to determine whether disrupting the CLC-7/Ostm1 TMD interface affects voltage-dependent activation (*30*). Cells overexpressing $Ostm1^{Y300A}$, $CLC\text{-}7^{E416A}$, and $CLC\text{-}7^{E416A}$/$Ostm1^{Y300A}$ exhibited similarly slow activation kinetics compared to cells expressing the corresponding WT proteins, but all of the cells displayed reduced currents (Fig. 2, F and G). We noted that the current reduction for the $CLC\text{-}7^{E416A}$ and $CLC\text{-}7^{E416A}$/$Ostm1^{Y300A}$ mutants was more pronounced (Fig. 2F), consistent with the observed reduced surface protein level in $CLC\text{-}7^{E416}$ and $CLC\text{-}7^{E416A}$/$Ostm1^{Y300A}$ mutants (fig. S5, B and C). Collectively, these results validate our observations from the CLC-7/Ostm1 complex about specific residues that participate in the TMD interactions that stabilize the CLC-7/Ostm1 complex and show that disrupting the TMD interactions of CLC-7/Ostm1 reduces its current amplitude without altering the voltage-dependent slow gating activation.

The ion transport pathway of CLC-7

The ion transport pathway of CLC-7 resembles the shape of an hourglass and is constricted by a selectivity filter located in the middle

of the CLC-7 TMD. The N termini of α helices F, N, and D point toward the transport pathway and generate an electrostatically positive environment to attract negative ions (fig. S6A). There is no density for Cl^- ions in our CLC-7 structure. Distinct chloride binding sites (external site, S_{ext}; central site, S_{cen}; and internal site, S_{int}) are assigned on the basis of amino acid conservation among different CLC proteins (fig. S6, A to F). The proposed S_{ext} binding site of CLC-7 is established by the main-chain amide groups of Val^{513} and Phe^{514} from helix N, and Lys^{246} and Glu^{247} from helix F. The proposed S_{cen} binding site is formed by side-chain hydroxyl groups of Tyr^{602} and Ser^{204}, as well as main-chain amide groups of Gly^{512} and Val^{513}. The main-chain amide groups of Ser^{204} and Gly^{205} together comprise the proposed S_{int} binding site of CLC-7 (fig. S6A).

The gate glutamate in CLC proteins plays an indispensable role in H^+-coupled ion transport (*12*), because deprotonation of this glutamate impels the side chain of the carboxylic moiety to occupy the binding sites of S_{ext} or S_{cen}, thus preventing the binding of Cl^- ions. However, we were not successful in building an unbiased side chain of gate glutamate (E247) in CLC-7 due to radiation damage in our cryo-EM study. We noted that the conformation of Ser_C in the αC-D loop of CLC-7 resembles those of other CLC proteins (CLC-1, CmCLC, and EcCLC) but stands in contrast to the unique "flipped-down" conformation observed in CLC-K (fig. S6G) (*13*). Counting down toward the intracellular vestibule, in CLC-7, Glu^{314} from helix H, Tyr^{602} from helix L, and Met^{562} together constitute the intracellular constricted sites (fig. S6, H to L). The essential functions of the gating glutamate (Glu^{247}) and proton glutamate (Glu^{314}) in CLC-7 during transport have been demonstrated in a previous study: The CLC-7^{E247A} mutation resulted in almost ohmic, time-independent currents, while the CLC-7^{E314A} mutation reduced currents to background levels (*7*).

Interface between the N terminus, TMD, and CBS domains of CLC-7

Previous studies (*31*, *32*) have identified a point mutation (Y99C) at the N terminus of CLC-7 in patients with osteopetrosis. It is notable that N termini were absent in the previously resolved CLC proteins (*11*–*15*) largely due to flexibility. In our CLC-7 structure, it is noteworthy that a CLC-7 loop comprising the N-terminal (92–106) residues preceding helix A in CLC-7 protrudes into a cleft between CLC-7's TMD and CBS domains (Fig. 3A). Moreover, these cleft-residing residues form polar interactions with both the TMD and CBS2 domain within each of the CLC-7 monomers. In CLC-7, Tyr^{99} from the N-terminal loop interacts with Asp^{287} from the CLC-7 TMD, while the additional N-terminal loop residues Glu^{95}, Asp^{98}, and Asn^{104} interact with Asn^{659}, Arg^{767}, and Gln^{683} from the CBS2 domain (Fig. 3B). In addition, Asn^{214} from the TMD forms polar interactions with the neighboring Arg^{762} and Arg^{784} from the CBS domain.

Our CLC-7 structure offers a plausible explanation to help understand previous works about the Y99C mutant. That is, we now understand that the mutation disrupts the interaction between the N terminus and the TMD, thus affecting the transporter function. In contrast to other structurally resolved CLC proteins, the N-terminal loop of CLC-7 fills the cleft between TMD and CBS domains, thereby promoting the stabilization of the TMD and CBS domains via substantial interactions. The critical role of residues positioned at this CLC-7 cleft was initially proposed because a study identified clustering of several osteopetrosis-related mutations that result in accelerated ion transport activation kinetics, such as R286Q, R762Q, R762L, and R767Q (*7*). Our insights about this CLC-7 domain interface corroborate the previous finding and extend our understanding by the identification of the crucial function of the N terminus. A previous study established that separate expression of the CLC-7 CBS domains—both the domains alone and as fusion domains attached directly to Ostm1—could rescue the function of CLC-7 mutant variants with truncated CBS domains (*30*). However, a combination expression [$CLC\text{-}7_{\Delta CT}$ + $CLC\text{-}7_{CT(R762L)}$ + Ostm1] including the fast mutant R762L failed to yield currents (*30*), which was largely due to the perturbation of the interaction between the TMD and CBS domains.

The human CLC-7 and CLC-6 sequences share roughly 43% identity and 61% similarity. Sequence alignment suggests strong overlap between the potential interacting residues of CLC-6 and those we observed in our CLC-7 structure like Glu^{95}, Asp^{98}, Tyr^{99}, and Asn^{104} in the N-terminal loop, Asn^{214} in the TMD, as well as Arg^{762}, Arg^{767}, and Arg^{784} in the CBS domain (Fig. 3C). The sequence alignment indicates that CLC-6 may adopt a similar interaction between the N terminus, TMD, and CBS domains. Comparison of human CLC transporters (CLC-3 to CLC-7) highlights that residues like Asp^{98}, Arg^{762}, and Arg^{767} of CLC-7 are conserved in all these transporters (Fig. 3C), suggesting the potential for the analogous interaction modes among human CLC transporters. It is plausible that possible disease-causing mutations among the interface between the N terminus, TMD, and CBS domains could work through a similar mechanism, which awaits further investigations.

Slow gating mechanism of the CLC-7/Ostm1 complex

Previous studies of CLCs have demonstrated that the loop intervening helices D and E, together with the conformational changes in the CBS domains, affects the slow gating process of the CLC proteins (*15*, *33*, *34*). It is therefore plausible that slow gating may require coordinated conformational changes in both subunits of CLC proteins, with these changes affecting the domain interaction interface. To better characterize the slow gating mechanism of the CLC-7/Ostm1 complex, we investigated the voltage-dependent activation of the CLC-7/Ostm1 complex by generating mutant variants of CLC-7 for the TMD, CBS domain, and N terminus (Fig. 4, fig. S7, and table S2). Guided by a previous study (*7*), note that all of these CLC-7 mutant variants additionally carried the leucine mutations that partially target CLC-7 to the plasma membrane.

The dimeric architecture of CLC-7 is stabilized by interactions contributed by CLC-7's TMD, N terminus, and CBS domains (Fig. 4A). To investigate the importance of the N terminus interaction, six representative polar amino acids of the N-terminal loop (Glu^{95}, Ser^{96}, Asp^{98}, Tyr^{99}, Ser^{102}, and Asn^{104}) that protrude into the interface were mutated to alanine (Fig. 4B and fig. S7A). The resultant S96A and S102A mutants were virtually unchanged compared to the WT CLC-7, whereas the other four mutants exhibited accelerated activation kinetics (Fig. 4B), which was possibly due to the disruption of the interaction of the interface. The N104A mutation caused a moderate increase in activation kinetics, whereas the E95A, D98A, and Y99A mutations resulted in fast activation kinetics, having time constant ($\tau_{activation}$) values more than threefold faster than WT CLC-7 (Fig. 4B and table S2). We also mutated residues Asn^{214} from TMD and Arg^{784} from the CBS domain (Fig. 3B and fig. S7B). Compared with WT CLC-7, both mutants (N214A and R784A) exhibited markedly accelerated $\tau_{activation}$ values (sixfold rate increase) (Fig. 4D and table S2).

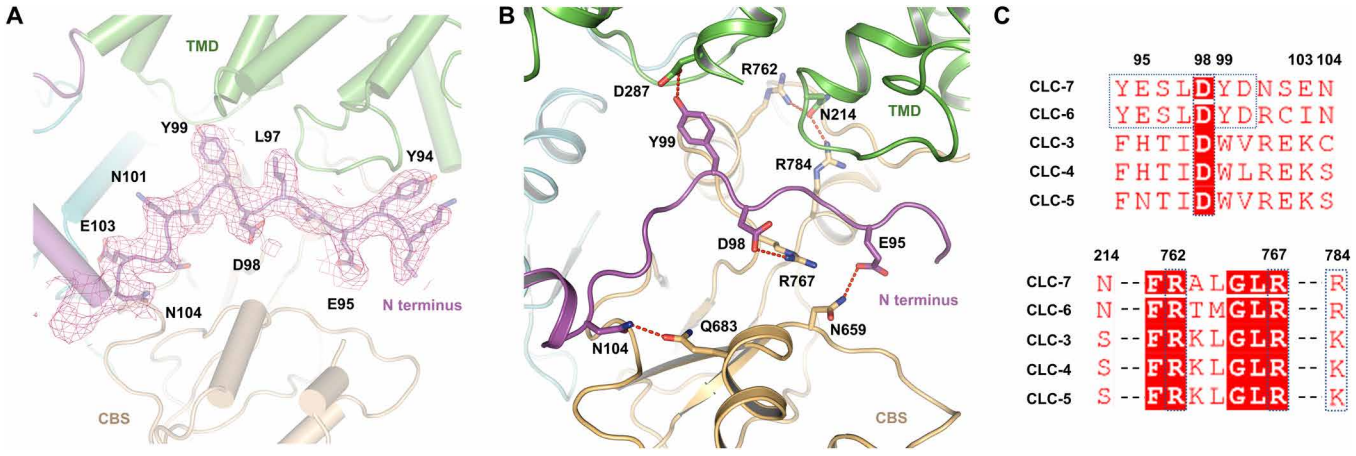

Fig. 3. An interface between the N terminus, TMD, and CBS domains. (**A**) Ribbon representation of the domain interface between N terminus, TMD, and CBS domains. Representative residues in the N terminus are shown with side chains. The EM density of the N terminus is shown at a contour level of 5σ. Purple, N terminus; green, TMD; brown, CBS domain. (**B**) Polar interactions in the domain interface between the TMD, CBS domain, and the N terminus of one CLC-7 monomer. Polar interactions were shown as dashed lines. Purple, N terminus; green, TMD; brown, CBS domain. (**C**) Sequence alignment of the N terminus, TMD, and CBS domain between human CLC-7 and other CLC transporters.

Counting down to the CBS domains, the dimer interface was contributed by the polar amino acids that Ser^{753}, Arg^{756}, Lys^{759}, and Asn^{774} from one monomer lay close to the adjacent Glu^{103}, Ser^{744}, Tyr^{746}, and Asn^{776} from another monomer (Fig. 4C). Representative residues (Arg^{756}, Tyr^{746}, and Glu^{103}) in the CBS dimer interface were mutated to alanine (fig. S7, A and B), which accelerated the activation kinetics (Fig. 4, C and D, and table S2), indicating that the CBS dimer interface is also involved in voltage-dependent activation.

Of additional importance at the TMD in CLC-7, Glu^{313} from one CLC-7 monomer interacts with Gln^{321} from the neighboring monomer to stabilize the dimeric TMD (Fig. 4E). To assess whether the TMD interface also participates in voltage-dependent activation, we subsequently mutated residues (Glu^{313} and Gln^{321}) involved in the TMD dimer interface (fig. S7C). The resultant single (E313A, Q321A) and double mutant (E313A/Q321A) variants exhibited accelerated voltage-dependent activation (Fig. 4F). For the double mutant (E313A/Q321A), the $\tau_{activation}$ value was increased by 20-fold (table S2), revealing additive impacts for mutation of these two residues. Moreover, these mutant variants (E313A, Q321A, and E313A/Q321A) showed a relatively slower deactivation process (fig. S7C) compared with the other accelerated mutant variants we examined, suggesting that the disruption of the TMD interaction somehow alters the transporter deactivation. Glu^{313} lies close to the proton glutamate Glu^{314}, and the disruption of Glu^{313} and Gln^{321} interaction may affect the proton transport in CLC-7/Ostm1, which may contribute to both slow gating and conductance of the CLC-7/Ostm1 complex.

DISCUSSION

Our structural elucidation of the CLC-7/Ostm1 complex lays a foundation for understanding the potential mechanism of pathogenic mutations in CLC-7. To date, among roughly 40 known osteopetrosis mutations in CLC-7 (*1*, *20*, *35*–*37*), 27 mutations can be mapped into our resolved CLC-7 structure (Fig. 5A), which could be further divided into three conceptual groups. (i) Mutations in the ion translocation pathway of CLC-7 were expected to affect ion transport (Fig. 5B). The P249L and G203D mutants are positioned near our predicted chloride coordinating sites and may therefore hamper the ion transport. A previous study reported that the D145G mutant accelerated the activation and relaxation kinetics of CLC-7 (*38*). Residue Asp^{145} is positioned in the intravesicular vestibule, and the D145G mutant may affect the ion transport function of CLC-7. (ii) Among the mapped disease mutations, residues at the CLC-7 domain interface between the TMD, CBS domain, and N terminus are the hotspot mutation sites (Fig. 5C), implying their notable roles of the domain interface in transporter regulation. The accelerated mutant residues (L213F, R286W, R762L, and R767W) are located at this interface (Fig. 5C). R286W, R762L, and R767W mutants directly change the charge of the domain interface. L213F mutant contains a bulky side chain and may affect the neighboring interacting residues, like Asn^{214}. Moreover, consecutive residue (313–318) mutations were observed in osteopetrosis because these residues may affect the function of the proton glutamate Glu^{314} (Fig. 5C). (iii) Mutations in the CBS dimer interface of CLC-7 may affect the CBS interaction and slow gating, like the R674Q, G677V, and Y746Q mutants (Fig. 5D). Particularly, mutagenesis of the Tyr^{746} residue accelerates the kinetic activation by fivefold compared with WT activity (Fig. 4D), in accord with the homologous osteopetrosis-related cattle Y750Q mutant (*37*). In addition, a mutation in CLC-7 causes a lysosomal storage disorder but does not lead to osteopetrosis (*24*); specifically, the gain-of-function mutation Y715C enhanced CLC-7 activity and altered the lysosomal pH (*24*). Our structure shows that Tyr^{715}, which is located in the CBS2 domain of CLC-7, forms hydrogen bonds with Asp^{282} from the TMD (fig. S8). Thus, it appears likely that the Y715C mutation alters the interaction between the CLC-7 TMD and CBS domains, resulting in an accelerated activation kinetics consistent with previously reported electrophysiology currents (*24*).

It has been reported that glycosylation helps protect endolysosomal membrane proteins from degradation (*29*). In vivo instability of CLC-7 proteins was observed in the absence of Ostm1 (*19*), raising the possibility that Ostm1 may shield CLC-7 from degradation by lysosomal proteases. Our CLC-7/Ostm1 structure corroborates this previously proposed hypothesis from the structural side as the highly

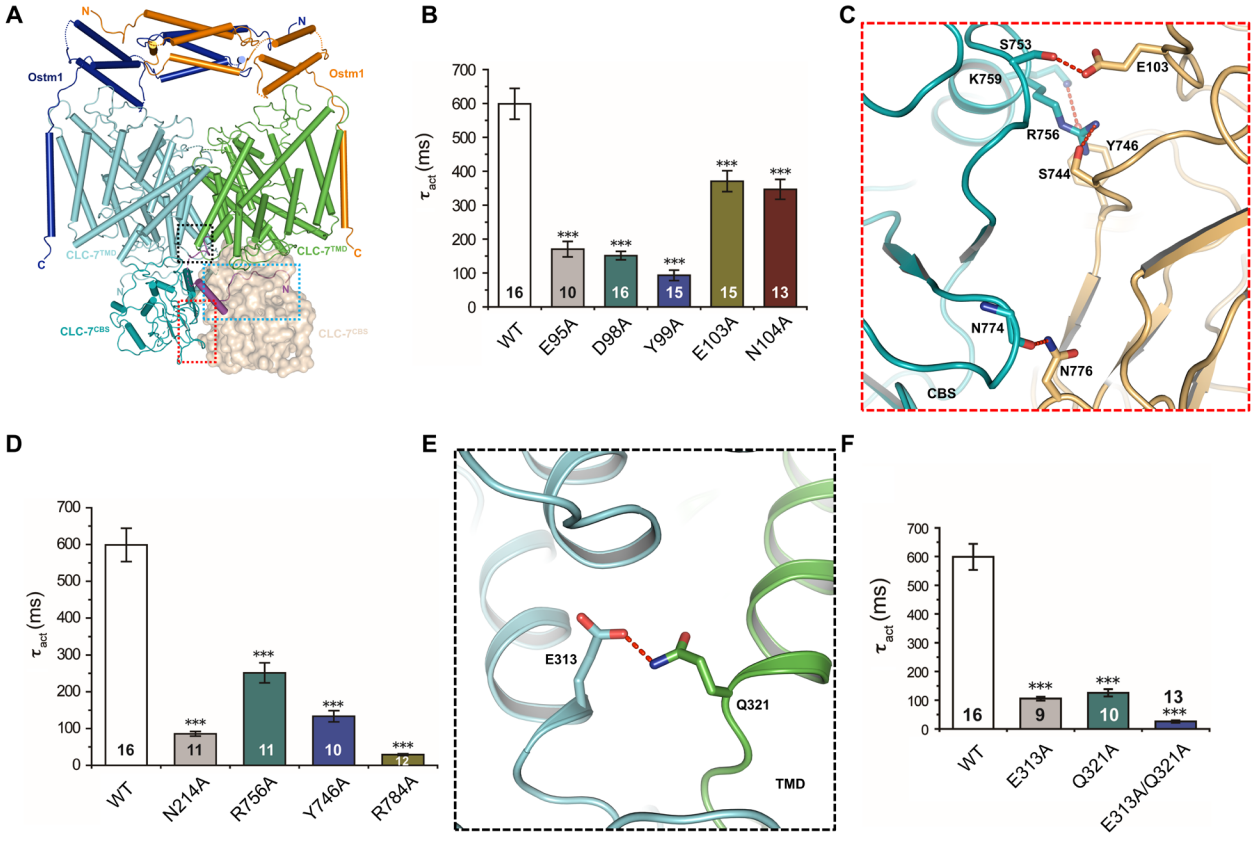

Fig. 4. Dimer interface and domain interaction in CLC-7. (**A**) Ribbon representation of the CLC-7/Ostm1 complex, with each subunit color-coded. The N terminus of one CLC-7 monomer was shown in purple, and the CBS domain of one monomer was shown in the surface for clarity. Three dashed boxes were represented to show the domain interaction within CLC-7 (black box, TMD; red box, CBS domain; green box, N terminus). (**B**) Bar graphs of the activation time constant ($\tau_{activation}$) of the N-terminal mutants. The $\tau_{activation}$ values were measured at +140 mV. Data are represented as means ± SEM. The inserted numbers in the bar represent the independent experimental times in each group. (**C**) Magnified view of the polar interactions between the CBS domain of CLC-7. Polar interactions were shown as dashed lines. (**D**) Bar graphs of the activation time constant of the CBS domain mutants. The $\tau_{activation}$ values were measured at +140 mV. Data are represented as means ± SEM. The inserted numbers in the bar represent the independent experimental times in each group. (**E**) Magnified view of the polar interactions between the TMD of CLC-7. Polar interactions were shown as dashed lines. (**F**) Bar graphs of the activation time constant of the TMD mutants. The $\tau_{activation}$ values were measured at +140 mV. Data are represented as means ± SEM. The inserted numbers in the bar represent the independent experimental times in each group.

glycosylated Ostm1 is positioned as a shield over the nonglycosylated CLC-7 (Fig. 2B). Moreover, as illustrated in fig. S4B, the surface of the intravascular domain of CLC-7 is charged, providing an opportunity to interact with dendritic glycan moieties (N263-NAG and N163-NAG) in the interface cleft between Ostm1 and CLC-7 (fig. S4B). We cannot rule out the possibility that, under physiological conditions, these sugars might form carbohydrate-carbohydrate or carbohydrate-protein interactions; it is difficult to assign any such interactions based on our structural model due to flexibility.

Compared with the well-established fast gating process of CLC proteins, the slow gating process on both pores of CLC proteins remains enigmatic (*9*, *16*, *17*). A previous study used cleverly designed experiments featuring coexpressions of WT and fast mutant subunits (*30*) to support the idea that the slow gating of CLC-7/Ostm1 underlying the voltage-dependent activation was dependent on the interaction between the CBS domain and the TMD of CLC-7. Supporting this, our CLC-7/Ostm1 structure and our functional electrophysiology results demonstrate that mutations in the CLC-7 TMD, CBS domain, and N terminus accelerate slow gating (Figs. 4 and 6 and fig. S7). That is, our work moderately extends the understanding of the slow gating process by establishing a requirement for coordinated conformational changes in these regions of the CLC-7/Ostm1 complex (Figs. 4 and 6 and fig. S7). Congruent with the previously reported large movement of the CLC-7 C terminus observed in fluorescence resonance energy transfer (FRET) experiments (*39*), our mutagenesis of residues at the CBS domain interface (Fig. 4, C and D) further illustrate how conformational changes in the opposing CBS domain functionally affect the slow gating process. The substantial interactions we identified within the TMD, CBS domain, and N terminus of CLC-7 collectively contribute to increasing the energetic threshold required to stimulate voltage-dependent activation, thereby helping explain the slow gating process. That is, CLC-7 stability confers a high kinetic barrier for activation, and we show that disruption of stability-increasing interactions at the domain interface decreases the kinetic barrier, which results in acceleration of voltage-dependent activation (fig. S7).

Collectively, we present the structure of the human CLC-7/Ostm1 complex and several features were observed to ravel the distinct characteristics of CLC-7 when compared with other CLC proteins, including the interactions between CLC-7 with auxiliary domain

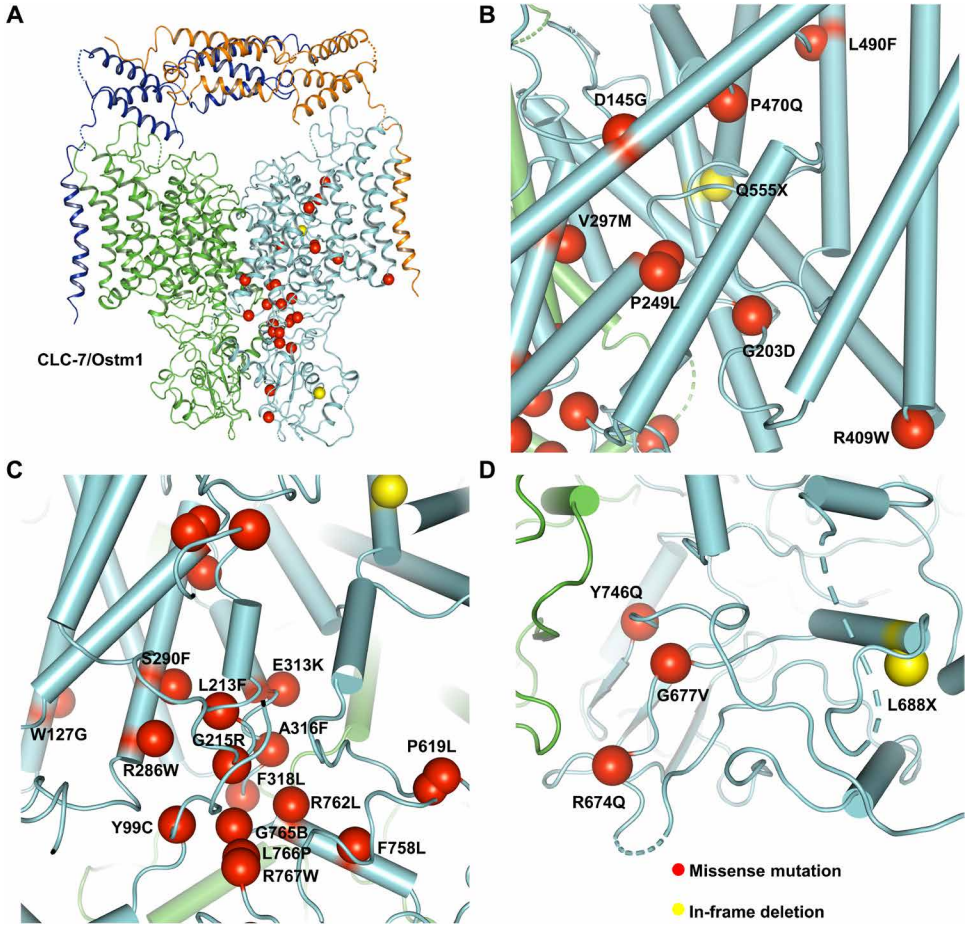

Fig. 5. Mapping of the osteopetrosis related mutations. (**A**) Structural mapping of the pathogenic osteopetrosis mutations in CLC-7/Ostm1 complex. (**B**) Close-up view of the mutations in the TMD of CLC-7 monomer. (**C**) Close-up view of the mutations in the interface cleft between the N terminus, CBS domain, and the TMD of CLC-7 monomer. (**D**) Close-up view of the mutations in the CBS domain of CLC-7 monomer.

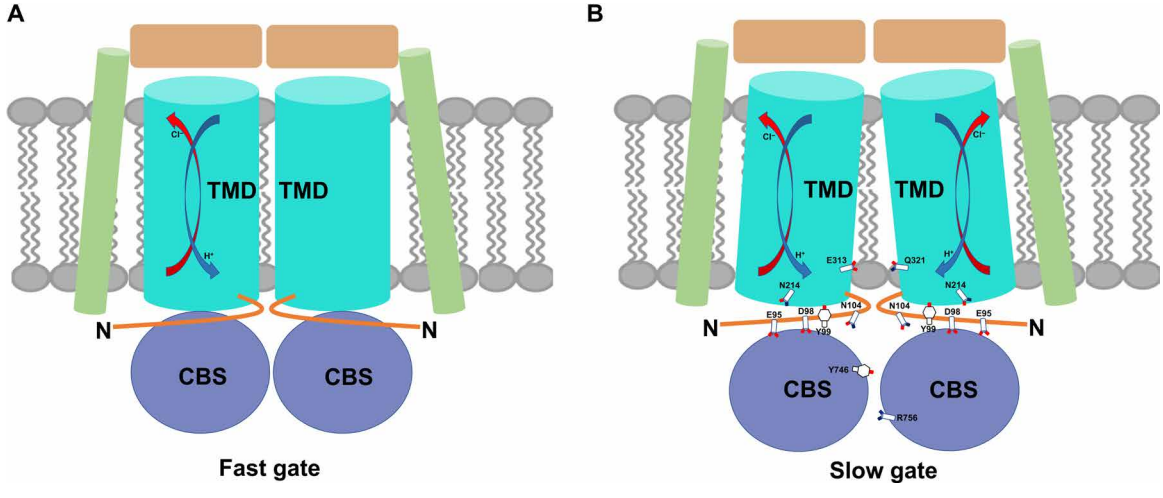

Fig. 6. Cartoon model for the fast gate and the slow gate of CLC-7/Ostm1. (**A**) Fast gate of CLC-7/Ostm1 was largely related to the small movement of gate glutamate in the TMD. (**B**) Slow gate of CLC-7/Ostm1 requires a coordinated conformational change in the domain of both subunits, including the TMD, CBS domain, and N terminus. Representative interacting residues within the domain interface were shown as ribbons for clarity.

Ostm1 and the domain interface between the N terminus, TMD, and CBS domains, which helps understand the roles of CLC-7/Ostm1 and may serve as a starting point for finding drugs to treat osteopetrosis.

MATERIALS AND METHODS

Cell culture and transfection

Plasmids encoding *Homo sapiens* CLC-7 and Ostm1 were gifts from J. Han (Xiamen University, China). For protein expression, *H. sapiens* CLC-7 was cloned in frame with a C-terminal tandem twin Strep-tag into the pEG BacMam vector, while Ostm1 was constructed into the vector with no tag. The BacMam viruses were produced and amplified to P2 (the second passage) virus from Sf9 cells (Invitrogen). Human embryonic kidney (HEK) 293F cells were cultured in SMM 293T-I medium (Sino Biological Inc.) under 8% CO_2 in a Multitron-Pro Shaker (Infors, 120 rpm) at 37°C. When the cell density reached 2×10^6 cells per milliliter, for the transfection of CLC-7/Ostm1 complex, the cell was transfected with the P2 BacMam viruses of CLC-7 and Ostm1, each at 15 ml per liter of cell culture. Sodium butyrate was added at a final concentration of 10 mM to the cell culture. The transfected cells were cultured for 48 hours before harvest. HEK293F cells (R79007) were purchased from Thermo Fisher Scientific Inc., and all experiments were performed in compliance with the institutional guidelines of the Tsinghua University and Shanghai Institute of Materia Medica, Chinese Academy of Sciences.

Protein expression and purification

For the protein purification of the CLC-7/Ostm1 complex, 2 liters of transfected HEK293F cells was harvested by centrifugation at 3000*g*. Cell pellets were resuspended in lysis buffer containing 20 mM Hepes (pH 7.4) and 150 mM NaCl, leupeptin (1 μg/ml), pepstatin (1.5 μg/ml), aprotinin (0.84 μg/ml), 0.3 mM phenylmethylsulfonyl fluoride and lysed by sonication for 5 min. The cell membrane was pelleted after a 100,000*g* ultracentrifugation for 1 hour. The membrane was resuspended in buffer containing 20 mM Hepes (pH 7.4), 150 mM NaCl, 2 mM dithiothreitol (DTT), and 1% (w/v) digitonin for 2 hours with gentle rotation at 4°C. After ultracentrifugation at 100,000*g* for 20 min, the supernatant was incubated with Strep-Tactin Sepharose (IBA) for 1 hour with gentle rotation at 4°C. The resin was washed extensively with wash buffer containing 20 mM Hepes (pH 7.4), 150 mM NaCl, 2 mM DTT, and 0.1% (w/v) digitonin. The target CLC-7/Ostm1 complex was eluted with wash buffer plus 5 mM D-desthiobiotin (IBA) and concentrated to a final volume of approximately 100 μl. The final protein was applied to size-exclusion chromatography (Superpose-6 10/300 GL, GE Healthcare) in buffer containing 20 mM Hepes (pH 7.4), 150 mM NaCl, and 0.1% digitonin. The peak corresponding to the CLC-7/Ostm1 complex was collected for further cryo-microscopy analysis.

Cryo–electron microscopy

The cryo-EM grids were prepared using Vitrobot Mark IV (FEI) operated at 4°C and 100% humidity. For samples of CLC-7/Ostm1, 4-μl aliquots of samples at concentrations of approximately 8 mg/ml were applied onto glow-discharged holey carbon grids (Quantifoil R1.2/1.3) 300 mesh Au grid. After a waiting time of 5 s, the grids were blotted for 2 s and plunged into liquid ethane for quick freezing.

The cryo-EM grids were screened on a Tecnai Arctica microscope (FEI) operated at 200 kV using a Falcon II 4k × 4k camera (FEI). The qualified grids were transferred into a Titan Krios microscope (FEI) operated at 300 kV for data acquisition, and the Gatan K2 Summit detector was equipped with a GIF Quantum energy filter. Images were automatically recorded using SerialEM with a slit width of 20 eV on the energy filter and in super-resolution mode at a nominal magnification of ×130,000, corresponding to a calibrated pixel size of 1.08 Å at object scale, and with defocus ranging from 1.3 to 2.3 μm. Each stack was exposed for 5.6 s with an exposing time of 0.175 s per frame, resulting in a total of 32 frames per stack, and the total dose rate for each stack was about 50 e/Å^2.

Image processing

The flowchart for data processing is summarized in fig. S1. For the dataset of CLC-7/Ostm1 complex, in total, 3956 micrographs (movie stacks) were collected for CLC-7/Ostm1 and were further processed by subregion motion correction and dose weighting using MotinCor2, generating summed micrographs with or without dose weighting. CTFFIND4 was used to estimate the contrast transfer function (CTF) parameters and produce the CTF power spectrum on the basis of summed micrographs from MotionCor2. Particles were auto-picked using Relion3.0 (*40*). For the dataset of CLC-7/Ostm1, ~1000 particles were manually picked in advance and processed by two-dimensional (2D) classification using Relion3.0. The resulting 2D averages were served as the templates for particle picking. Two rounds of 2D classifications were performed to exclude noise and other bad particles. Particles (1,251,000) from qualified 2D averages were selected for further 3D analysis. Ahead of 3D classification, a round of refinement was applied on the whole particle sets using Relion3.0. Three rounds of 3D classification with C1 symmetry generated 148,000 particles with good signal, and we omitted the bad particles. Gctf was used to refine the local defocus parameters. Aiming at to get higher resolution, the resultant particles were re-centered and processed by auto-refine with soft mask and C2 symmetry imposed using Relion3.0. Last, we get a 3.7-Å resolution map with C2 symmetry (fig. S1D). The local resolution map was calculated using ResMap and displayed in Chimera.

Model building

Models of full-length human CLC-7/Ostm1 were predicted on I-TASSER server. The predicted models were docked into the cryo-EM map with a resolution of 3.7 Å in Chimera and manually adjusted in Coot to acquire the atomic model of CLC-7/Ostm1. Sequence alignment and secondary structure prediction of CLC-7/Ostm1 were used to aid the model building. Model refinement was performed on the main chain of the two atom models using real_space_refine module of PHENIX with secondary structure and geometry restraints to avoid overfitting. The geometry of the models was evaluated by MolProbity.

For cross-validation against overfitting, we randomly displaced the atom positions of the final model by up to a maximum of 0.5 Å and refined against the half map 1 generated by Relion 3D auto-refine procedure, resulting in a model named Test. Then, we calculated the Fourier shell correlation (FSC) curve of both half map against the model Test and compared with the FSC curve of the final model against the summed map generated by Relion 3D auto-refine procedure.

In vitro pull-down assay

To facilitate the verification of CLC-7 and Ostm1 interaction, we generate a plasmid of CLC-7 containing a C-terminal Strep-tag and a plasmid of Ostm1 with a C-terminal Flag tag. Point mutations

were introduced by polymerase chain reaction, and the resultant constructs were CLC-7(E416A) and Ostm1(Y300A). In brief, we transfect 50-ml HEK293F cells with the following combinations: WT CLC-7 and WT Ostm1, WT CLC-7 and Y300A (Ostm1), E416A (CLC-7) and WT Ostm1. Transfected cells were lysed in 1-ml lysis buffer [25 mM tris (pH 7.8), 150 mM NaCl, 1 mM EGTA, cOmplete protease inhibitors] with 1% digitonin. The cell lysate was incubated for 30 min on ice and centrifuged for 10 min at 4°C at 20,000*g*. The supernatant was incubated with anti-Strep magnetic agarose (Thermo Fisher Scientific) for 2 hours at 4°C. The beads were collected on the magnet, washed three times with 1 ml of lysis buffer containing 0.1% digitonin, and eluted with 150 μl of SDS-gel loading buffer for Western blot. The same procedure was performed in the in vitro Flag-tag–mediated pull-down assay using the anti-Flag magnetic beads (Thermo Fisher Scientific). For Western blot analysis, proteins were subjected to a 4 to 20% SDS–polyacrylamide gel electrophoresis gel (GenScript) and transferred onto a polyvinylidene difluoride membrane (Millipore). Membranes were detected with the indicated antibodies. The primary antibodies Flag (Easybio) and Strep (Easybio) were used.

Whole-cell and cell-attach patch-clamp experiments

All the CLC-7 constructs in voltage-clamp assay were subcloned into the pcDNA3.1(−) vector and additionally carry the di-leucine (LL23/24AA, LL68/69AA) mutation introduced by point mutation to partially target CLC-7 to the plasma membrane. Ostm1 was subcloned in frame with a C-terminal GFP into the pEGFP-N1 vector. CHO cells were cultured in Dulbecco's modified Eagle's medium (Thermo Fisher Scientific) supplemented with 10% fetal bovine serum (Gibco) and 1% penicillin-streptomycin solution under 5% CO_2 at 37°C incubator. All whole-cell patch-clamp recording and cell-attach recording in CHO were conducted 48 to 72 hours after transfection with Axopatch 200B (Molecular Devices) under room temperature (~23°C). The pipette was pulled with micropipette puller (P-97; Sutter Instrument) with 3- to 5-megohm resistance. Whole-cell recording and cell-attach recording were all performed under solution conditions with 110 mM CsCl, 10 mM NaCl, 0.5 mM $CaCl_2$, 1 mM EGTA, 2 mM Mg–adenosine 5′-triphosphate, and 40 mM Hepes (pH 7.2) in pipette, and 130 mM NaCl, 5 mM KCl, 1 mM $MgCl_2$, 1 mM $CaCl_2$, 10 mM glucose, and 20 mM Hepes (pH 7.4) with NaOH in bath. The whole-cell currents were evoked by clamping the cells for 2 s to voltages between −80 and 140 mV in 20-mV steps followed by a repolarizing step to −80 mV for 500 ms. The cell-attach single-channel recordings were obtained within clamped −80 to +80 mV under gap-free voltage-clamp program. Voltage-dependent currents and single-channel amplitudes were measured using Clampfit 10.2 Software.

To determine the activation kinetic changes of mutants, the activation time constant ($\tau_{activation}$) of currents was analyzed. We selected the first 500 ms of depolarization (+140 mV) fitting to a single exponential function:

$$I = Ae^{-t/\tau} + C$$

where I is the current amplitude, t is the time, A is the amplitude constant, and τ is the time constant. Last, the τ value at +140 mV between mutants and WT CLC-7 was compared.

Statistical analysis

The results were expressed as means ± SEM. The activation time constant ($\tau_{activation}$) changes of mutants were analyzed by unpaired Student's t test (comparing to WT CLC-7/Ostm1). Results were evaluated to be statistically significant when $P < 0.05$ or 0.01.

SUPPLEMENTARY MATERIALS

Supplementary material for this article is available at http://advances.sciencemag.org/cgi/content/full/6/33/eabb4747/DC1

View/request a protocol for this paper from *Bio-protocol*.

REFERENCES AND NOTES

1. T. J. Jentsch, M. Pusch, Clc Chloride channels and transporters: Structure, function, physiology, and disease. *Physiol. Rev.* **98**, 1493–1590 (2018).
2. T. J. Jentsch, Discovery of CLC transport proteins: Cloning, structure, function and pathophysiology. *J. Physiol.* **593**, 4091–4109 (2015).
3. T. J. Jentsch, L. Neagoe, O. Scheel, CLC chloride channels and transporters. *Curr. Opin. Neurobiol.* **15**, 319–325 (2005).
4. T.-Y. Chen, Structure and function of CLC channels. *Annu. Rev. Physiol.* **67**, 809–839 (2005).
5. O. Scheel, A. A. Zdebik, S. Lourdel, T. J. Jentsch, Voltage-dependent electrogenic chloride/proton exchange by endosomal CLC proteins. *Nature* **436**, 424–427 (2005).
6. A. Picollo, M. Pusch, Chloride/proton antiporter activity of mammalian CLC proteins ClC-4 and ClC-5. *Nature* **436**, 420–423 (2005).
7. L. Leisle, C. F. Ludwig, F. A. Wagner, T. J. Jentsch, T. Stauber, ClC-7 is a slowly voltage-gated $2Cl^-/1H^+$-exchanger and requires Ostm1 for transport activity. *EMBO J.* **30**, 2140–2152 (2011).
8. I. Neagoe, T. Stauber, P. Fidzinski, E.-Y. Bergsdorf, T. J. Jentsch, The late endosomal CLC-6 mediates proton/chloride countertransport in heterologous plasma membrane expression. *J. Biol. Chem.* **285**, 21689–21697 (2010).
9. C. Miller, M. M. White, Dimeric structure of single chloride channels from torpedo electroplax. *Proc. Natl. Acad. Sci. U.S.A.* **81**, 2772–2775 (1984).
10. U. Ludewig, M. Pusch, T. J. Jentsch, Two physically distinct pores in the dimeric ClC-0 chloride channel. *Nature* **383**, 340–343 (1996).
11. R. Dutzler, E. B. Campbell, M. Cadene, B. T. Chait, R. MacKinnon, X-ray structure of a ClC chloride channel at 3.0 Å reveals the molecular basis of anion selectivity. *Nature* **415**, 287–294 (2002).
12. L. A. Feng, E. B. Campbell, Y. C. Hsiung, R. MacKinnon, Structure of a eukaryotic CLC transporter defines an intermediate state in the transport cycle. *Science* **330**, 635–641 (2010).
13. E. Park, E. B. Campbell, R. MacKinnon, Structure of a CLC chloride ion channel by cryo-electron microscopy. *Nature* **541**, 500–505 (2017).
14. E. Park, R. MacKinnon, Structure of the CLC-1 chloride channel from *Homo sapiens*. *eLife* **7**, e36629 (2018).
15. K. T. Wang, S. S. Preisler, L. Zhang, Y. Cui, J. W. Missel, C. Grønberg, K. Gotfryd, E. Lindahl, M. Andersson, K. Calloe, P. F. Egea, D. A. Klaerke, M. Pusch, P. A. Pedersen, Z. H. Zhou, P. Gourdon, Structure of the human ClC-1 chloride channel. *PLOS Biol.* **17**, e3000218 (2019).
16. C. K. Bauer, K. Steinmeyer, J. R. Schwarz, T. J. Jentsch, Completely functional double-barreled chloride channel expressed from a single torpedo cDNA. *Proc. Natl. Acad. Sci. U.S.A.* **88**, 11052–11056 (1991).
17. U. Ludewig, M. Pusch, T. J. Jentsch, Independent gating of single pores in CLC-0 chloride channels. *Biophys. J.* **73**, 789–797 (1997).
18. D. Kasper, R. Planells-Cases, J. C. Fuhrmann, O. Scheel, O. Zeitz, K. Ruether, A. Schmitt, M. Poët, R. Steinfeld, M. Schweizer, U. Kornak, T. J. Jentsch, Loss of the chloride channel ClC-7 leads to lysosomal storage disease and neurodegeneration. *EMBO J.* **24**, 1079–1091 (2005).
19. P. F. Lange, L. Wartosch, T. J. Jentsch, J. C. Fuhrmann, ClC-7 requires Ostm1 as a β-subunit to support bone resorption and lysosomal function. *Nature* **440**, 220–223 (2006).
20. U. Kornak, D. Kasper, M. R. Bösl, E. Kaiser, M. Schweizer, A. Schulz, W. Friedrich, G. Delling, T. J. Jentsch, Loss of the ClC-7 chloride channel leads to osteopetrosis in mice and man. *Cell* **104**, 205–215 (2001).
21. J. A. Mindell, Lysosomal acidification mechanisms. *Annu. Rev. Physiol.* **74**, 69–86 (2012).
22. T. J. Jentsch, V. Stein, F. Weinreich, A. A. Zdebik, Molecular structure and physiological function of chloride channels. *Physiol. Rev.* **82**, 503–568 (2002).
23. S. Weinert, S. Jabs, C. Supanchart, M. Schweizer, N. Gimber, M. Richter, J. Rademann, T. Stauber, U. Kornak, T. J. Jentsch, Lysosomal pathology and osteopetrosis upon loss of H^+-driven lysosomal Cl- accumulation. *Science* **328**, 1401–1403 (2010).
24. E.-R. Nicoli, M. R. Weston, M. Hackbarth, A. Becerril, A. Larson, W. M. Zein, P. R. Baker II, J. D. Burke, H. Dorward, M. Davids, Y. Huang, D. R. Adams, P. M. Zerfas, D. Chen, T. C. Markello, C. Toro, T. Wood, G. Elliott, M. Vu; Undiagnosed Diseases Network, W. Zheng, L. J. Garrett, C. J. Tifft, W. A. Gahl, D. L. Day-Salvatore, J. A. Mindell, M. C. V. Malicdan, Lysosomal storage and albinism due to effects of a de novo *CLCN7* variant on lysosomal acidification. *Am. J. Hum. Genet.* **104**, 1127–1138 (2019).

25. N. Chalhoub, N. Benachenhou, V. Rajapurohitam, M. Pata, M. Ferron, A. Frattini, A. Villa, J. Vacher, Grey-lethal mutation induces severe malignant autosomal recessive osteopetrosis in mouse and human. *Nat. Med.* **9**, 399–406 (2003).
26. A. Fasth, Osteopetrosis—More than only a disease of the bone. *Am. J. Hematol.* **84**, 469–470 (2009).
27. C. Sobacchi, A. Schulz, F. P. Coxon, A. Villa, M. H. Helfrich, Osteopetrosis: Genetics, treatment and new insights into osteoclast function. *Nat. Rev. Endocrinol.* **9**, 522–536 (2013).
28. A. E. Coudert, M. C. de Vernejoul, M. Muraca, A. Del Fattore, Osteopetrosis and its relevance for the discovery of new functions associated with the skeleton. *Int. J. Endocrinol.* **2015**, 372156 (2015).
29. M. Fukuda, Lysosomal membrane glycoproteins. Structure, biosynthesis, and intracellular trafficking. *J. Biol. Chem.* **266**, 21327–21330 (1991).
30. C. F. Ludwig, F. Ullrich, L. Leisle, T. Stauber, T. J. Jentsch, Common gating of both CLC transporter subunits underlies voltage-dependent activation of the $2Cl^-/1H^+$ exchanger ClC-7/Ostm1. *J. Biol. Chem.* **288**, 28611–28619 (2013).
31. W. G. Sui, M. Ou, J. Liang, M. Ding, J. Chen, W. Liu, R. Xiao, X. Meng, L. Wang, X. Pan, P. Zhu, W. Xue, Y. Zhang, H. Lin, F. Li, J. Zhang, Y. Dai, Rapid gene identification in a Chinese osteopetrosis family by whole exome sequencing. *Gene* **516**, 311–315 (2013).
32. C. Supanchart, L. Wartosch, C. Schlack, J. Kühnisch, D. Felsenberg, J. C. Fuhrmann, M.-C. de Vernejoul, T. J. Jentsch, U. Kornak, ClC-7 expression levels critically regulate bone turnover, but not gastric acid secretion. *Bone* **58**, 92–102 (2014).
33. B. Wollnik, C. Kubisch, K. Steinmeyer, M. Pusch, Identification of functionally important regions of the muscular chloride channel ClC-1 by analysis of recessive and dominant myotonic mutations. *Hum. Mol. Genet.* **6**, 805–811 (1997).
34. B. J. Simpson, T. A. Height, G. Y. Rychkov, K. J. Nowak, N. G. Laing, B. P. Hughes, A. H. Bretag, Characterization of three myotonia-associated mutations of the CLCN1 chloride channel gene via heterologous expression. *Hum. Mutat.* **24**, 185 (2004).
35. E. Cleiren, O. Bénichou, E. Van Hul, J. Gram, J. Bollerslev, F. R. Singer, K. Beaverson, A. Aledo, M. P. Whyte, T. Yoneyama, M.-C. deVernejoul, W. Van Hul, Albers-Schönberg disease (autosomal dominant osteopetrosis, type II) results from mutations in the *ClCN7* chloride channel gene. *Hum. Mol. Genet.* **10**, 2861–2867 (2001).
36. Q. Pang, Y. Chi, Z. Zhao, X. Xing, M. Li, O. Wang, Y. Jiang, R. Liao, Y. Sun, J. Dong, W. Xia, Novel mutations of *CLCN7* cause autosomal dominant osteopetrosis type II (ADO-II) and intermediate autosomal recessive osteopetrosis (IARO) in Chinese patients. *Osteoporos. Int.* **27**, 1047–1055 (2016).
37. A. Sartelet, T. Stauber, W. Coppieters, C. F. Ludwig, C. Fasquelle, T. Druet, Z. Zhang, N. Ahariz, N. Cambisano, T. J. Jentsch, C. Charlier, A missense mutation accelerating the gating of the lysosomal Cl-/H^+-exchanger ClC-7/Ostm1 causes osteopetrosis with gingival hamartomas in cattle. *Dis. Model. Mech.* **7**, 119–128 (2014).
38. F. Barvencik, I. Kurth, T. Koehne, T. Stauber, J. Zustin, K. Tsiakas, C. F. Ludwig, F. T. Beil, J. M. Pestka, M. Hahn, R. Santer, C. Supanchart, U. Kornak, A. D. Fattore, T. J. Jentsch, A. Teti, A. Schulz, T. Schinke, M. Amling, *CLCN7* and *TCIRG1* mutations differentially affect bone matrix mineralization in osteopetrotic individuals. *J. Bone Miner. Res.* **29**, 982–991 (2014).
39. E. A. Bykova, X.-D. Zhang, T.-Y. Chen, J. Zheng, Large movement in the C terminus of CLC-0 chloride channel during slow gating. *Nat. Struct. Mol. Biol.* **13**, 1115–1119 (2006).
40. J. Zivanov, T. Nakane, B. O. Forsberg, D. Kimanius, W. J. Hagen, E. Lindahl, S. H. Scheres, New tools for automated high-resolution cryo-EM structure determination in RELION-3. *eLife* **7**, e42166 (2018).

Acknowledgments: We thank the Cryo-EM Facility Center of Southern University of Science & Technology (Shenzhen) and Tsinghua University Branch of China National Center for Protein Sciences (Beijing) for providing the facility support. The computation was completed on the Yang laboratory GPU workstation. **Funding:** This work was supported by funds from the National Key R&D Program of China (2017YFA0504600, 2016YFA0501100, and 2018ZX09711002), the Fundamental Research Funds for the Central Universities (22120180534), the Strategic Priority Research Program of the Chinese Academy of Sciences (XDA12040220), the National Science Fund for Distinguished Young Scholars (31625008), and the National Natural Science Foundation of China (21532004, 31570733, 81771188, 81901376, and 31671049). **Author contributions:** M.Y., Z.L., and Y.Li directed the study. S.Z., Y.Liu, and J.Z. did the protein purification and detergent screening. S.Z. and Y.Liu performed EM sample preparation, data collection, and structural determination with help of M.Y. Y.Liu and J.Z. performed the in vitro pull-down assay with the help of S.Z. B.Z. and T.L. performed the electrophysiology with the help of Y.Li and Z.L. M.Y., S.Z., Y.Liu, B.Z., and Z.L. built the model, drew the figures, and wrote the manuscript. All authors contributed to the discussion of the data and editing the manuscript. **Competing interests:** The authors declare that they have no competing interests. **Data and materials availability:** The 3D cryo-EM density map has been deposited in the Electron Microscopy Data Bank (EMDB), with accession code EMD 30238. The coordinates of atomic models have been deposited in the Protein Data Bank (PDB), with the accession code 7BXU. All data needed to evaluate the conclusions in the paper are present in the paper and/or the Supplementary Materials. Additional data related to this paper may be requested from the authors.

Submitted 26 February 2020
Accepted 29 June 2020
Published 12 August 2020
10.1126/sciadv.abb4747

Citation: S. Zhang, Y. Liu, B. Zhang, J. Zhou, T. Li, Z. Liu, Y. Li, M. Yang, Molecular insights into the human CLC-7/Ostm1 transporter. *Sci. Adv.* **6**, eabb4747 (2020).